Journal of Colloid and Interface Science 699 (2025) 138199

Contents lists available at ScienceDirect

Journal of Colloid And Interface Science

journal homepage: www.elsevier.com/locate/jcis

Regular Article

Differentially engineered nano-tracker of intracellular drug for potentiating breast cancer treatment

MiriGuli Musa [a,1], Xinxin Sun [b,1], Jianbin Shi [b], Jing Li [c,*], Shenwu Zhang [b,*], Xianbao Shi [a,*]

[a] Department of Pharmacy, The First Affiliated Hospital of Jinzhou Medical University, Jinzhou, China
[b] Department of Pharmaceutics, Wuya College of Innovation, Shenyang Pharmaceutical University, Shenyang 110016, China
[c] School of Pharmacy, Shenyang Medical College, Shenyang, Liaoning Province, China

HIGHLIGHTS

- Linker-free Art-TPE simplifies synthesis while preserving anti-tumor activity.
- Art-TPE NAs render a 2-fold AIE effect enhancement compared to TPE NAs.
- Nano-tracker can trace the release of intracellular drug in real time.

GRAPHICAL ABSTRACT

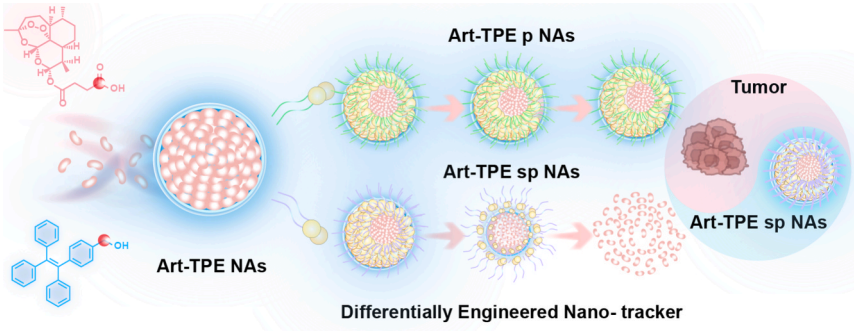

ARTICLE INFO

Keywords:
Art-TPE conjugate
Small-molecule assembly
Nano-tracker
AIE
Cancer therapy

ABSTRACT

Small-molecule self-assembled nanomedicines have shown considerable promise in anticancer therapy. However, the majority of these drugs are composed of the active drug, tumor-responsive chemical linkers, and assembly modules, which significantly complicate the synthesis process. Furthermore, the mechanisms underlying the cellular uptake and drug release of these tumor-responsive self-assembled nanodrugs remain unclear. To overcome these challenges, we exploit a differentially engineered nano-tracker, allowing real-time monitoring of changes in fluorescence intensity. The nano-tracker is elaborately self-assembled by a functional conjugate (artesunate-tetraphenylethylene, Art-TPE), which eliminates the sensitive linkers. Notably, such a functional conjugate not only retains effective anti-tumor activity, but renders a 2-fold aggregation-induced emission (AIE) effect enhancement compared to TPE. As expected, such a differentially engineered nano-tracker displays effective anti-tumor activity *in vitro* and *in vivo*. This study offers valuable insights into the development of small-molecule-based nanomedicines for more efficient diagnostic and therapeutic strategies.

* Corresponding authors.
E-mail addresses: dddefghijklmn@163.com (J. Li), zhangshenwu@aliyun.com (S. Zhang), sxbsln@163.com (X. Shi).
[1] These authors contributed equally to this work.

https://doi.org/10.1016/j.jcis.2025.138199
Received 21 March 2025; Received in revised form 13 June 2025; Accepted 13 June 2025
Available online 14 June 2025

1. Introduction

Malignant tumors, particularly breast cancer, represent a pressing global health challenge due to their escalating incidence and the complexity of therapeutic interventions [1–4]. Conventional chemotherapeutic agents, such as paclitaxel and doxorubicin, despite their extensive clinical utilization, are plagued by inherent limitations, including inadequate targeting specificity and severe systemic toxicity, which significantly compromise patients' quality of life [5]. In recent years, the natural compound artesunate (Art) has garnered substantial scientific interest owing to its distinctive anti-tumor mechanisms, such as the induction of oxidative stress and regulation of apoptotic pathways, demonstrating therapeutic potential in the management of breast cancer [6,7]. Nevertheless, the clinical translation of Art is hindered by its intrinsic physicochemical limitations, including poor aqueous solubility, short plasma half-life, and insufficient tumor-targeting capability, which collectively undermine its therapeutic efficacy [8–11]. Addressing these challenges through rational drug delivery strategies, while enabling real-time monitoring of drug distribution and release, has emerged as a critical frontier in advancing the precision and effectiveness of anticancer therapies.

In recent years, small-molecule self-assembled nanomedicines have emerged as a promising strategy to optimize drug delivery, addressing the inherent complexities and systemic toxicity associated with conventional nanoassembly-based systems [12–15]. Despite their significant advantages in tumor-targeting specificity and controlled drug release, conventional small-molecule self-assembly systems invariably necessitate a tripartite configuration comprising a therapeutic module, an assembly module, and an activation module, all of which are indispensable for functional integrity. Besides, the precise quantification of targeting efficiency and the synchronization of drug release kinetics remain formidable challenges, which impede the achievement of therapeutic precision. Previous studies have employed fluorescent probes to achieve precise drug quantification and tracking. However, this approach is limited by synthetic complexities and insufficient drug-loading efficiency, thereby failing to resolve the longstanding challenge of unclear intracellular and *in vivo* migration trajectories of nanodrugs. The advent of aggregation-induced emission (AIE) technology has introduced a paradigm-shifting solution to these limitations [16–18]. AIE-active molecules, leveraging their characteristic restricted intramolecular motion (RIM) mechanism, demonstrate a measurable exponential enhancement in fluorescence intensity upon the formation of nanoassemblies (NAs) [19–21]. This distinctive property facilitates real-time, *in situ* monitoring of nanomedicine dynamics: robust fluorescence signals delineate the transport trajectory of intact NAs, while fluorescence attenuation serves as a reliable indicator of drug release during nanostructure disassembly. In contrast to aggregation-caused quenching (ACQ) molecules, which suffer from fluorescence quenching upon aggregation, AIE technology enables "*in situ*, real-time, and quantitative" tracking of NAs disassembly through dynamic fluorescence signal modulation [22,23]. This technical refinement not only enhances the precision of drug delivery monitoring but also provides a robust platform for advancing the development of next-generation nanomedicines.

Owing to the rigid molecular architecture of Art, its intrinsic self-assembly capability is severely constrained, posing a significant obstacle to the direct construction of Art-based self-delivery system [24]. To address this limitation, the incorporation of modular groups endowed with programmable assembly properties is essential to facilitate nanoscale drug delivery. Tetraphenylethylene (TPE), a prototypical AIE luminogen, not only confers fluorescence tracing functionality to the nanostructure but also augments Art's intermolecular interactions through its distinctive non-planar, propeller-like conformation, thereby markedly enhancing the self-assembly propensity of Art [25,26]. Nevertheless, conventional strategies for connecting drug and assembly modules predominantly rely on the intricate "active drug-linker-assembly module" ternary composite design, which entails laborious synthetic procedures and is susceptible to premature drug release or off-target toxicity due to the inherent chemical lability of the linker. Intriguingly, we discovered that the direct conjugation of Art with TPE does not compromise its pharmacological activity [27]. The molecular framework of Art incorporates a peroxide bridge, a critical pharmacophoric element that remains stable throughout the self-assembly process, obviating the need for a linker and thereby preserving the drug's bioactivity [28]. This methodological improvement not only provides a systematic framework for streamlining nanomedicine design but also offers a theoretical foundation for the efficient delivery and functional retention of Art, paving the way for the development of advanced therapeutic platforms.

Building upon this foundation, we proposed a differentially engineered nano-tracker that seamlessly integrates the dual functionalities of "efficient drug loading" and "real-time tracking" (Fig. 1). By directly conjugating Art with TPE, we successfully constructed an Art-TPE conjugate molecule without the necessity of a linker. Significantly, the Art-TPE conjugate demonstrated the ability to spontaneously self-assemble into uniform NAs through a straightforward one-step nanoprecipitation method [29]. This approach significantly enhanced the assembly efficiency of Art, reducing the particle size from 342 nm to 188 nm, while simultaneously doubling the fluorescence intensity compared to TPE alone. To further optimize the system, DSPE-SS-PEG_{2K} was employed for surface modification to enhance NAs' stability during systemic circulation and facilitate disulfide bond cleavage in the high-glutathione (GSH) tumor microenvironment, thereby enabling tumor-specific drug release and synchronized fluorescence signal feedback [30–34]. This engineered design addressed the critical limitation of conventional systems, which lack the capability to monitor intracellular drug release in real time. The effective anti-tumor efficacy of Art-TPE was further validated in 4T1 tumor-bearing mice model, underscoring its therapeutic potential. This strategy not only provides an integrated design principle for the precise delivery of small-molecule self-assembled nanomedicines but also establishes a robust framework for efficient diagnostic and therapeutic strategies, representing a methodological progression in the field of nanomedicine.

2. Materials and methods

2.1. Materials

Both Art and TPE were purchased from Shanghai Bide Pharmaceutical Technology Co., Ltd. DSPE-PEG_{2K} was purchased from AVT (Shanghai) Pharmaceutical Tech Co., Ltd. EDCI (1-Ethyl-3-(3-dimethylaminopropyl) hydrochloride), HoBt (1-Hydroxybenzotriazole), and DMAP (4-Dimethylaminopyridine) were purchased from Energy Chemical (Anhui, China). DSPE-SS-PEG_{2K} was obtained from Xi'an Ruixi Biotechnology Co., Ltd. RPMI 1640 cell culture medium, DMEM cell culture medium, phosphate-buffered saline (PBS), fetal bovine serum (FBS), penicillin streptomycin, and trypsin-EDTA, and 3-(4,5-dimethyl-2-thiazolyl)-2,5-diphenyl-2H-tetrazolium bromide (MTT) were obtained from Dalian Meilun Biotechnology Co., Ltd., China. The live/dead cell staining kit was from Shanghai Beibo Biotechnology Co., Ltd. A reactive oxygen species (ROS) assay kit (DCFH-DA) was purchased from Glenview. All vessels for cell culture were supplied by Wuxi NEST Biotechnology Co., Ltd., China, and any other solvents and chemicals are analytical grade or HPLC grade.

2.2. Design and synthesis of Art-TPE

Art (0.83 mmol) and TPE (0.83 mmol) were dissolved in 10 mL of dichloromethane. Subsequently, EDCI (2 mmol), HoBt (1 mmol), and DMAP (0.2 mmol) were added sequentially, and the reaction mixture was stirred at 25 °C under a nitrogen atmosphere for 48 h. The reaction progress was monitored by thin-layer chromatography (TLC). After 48 h,

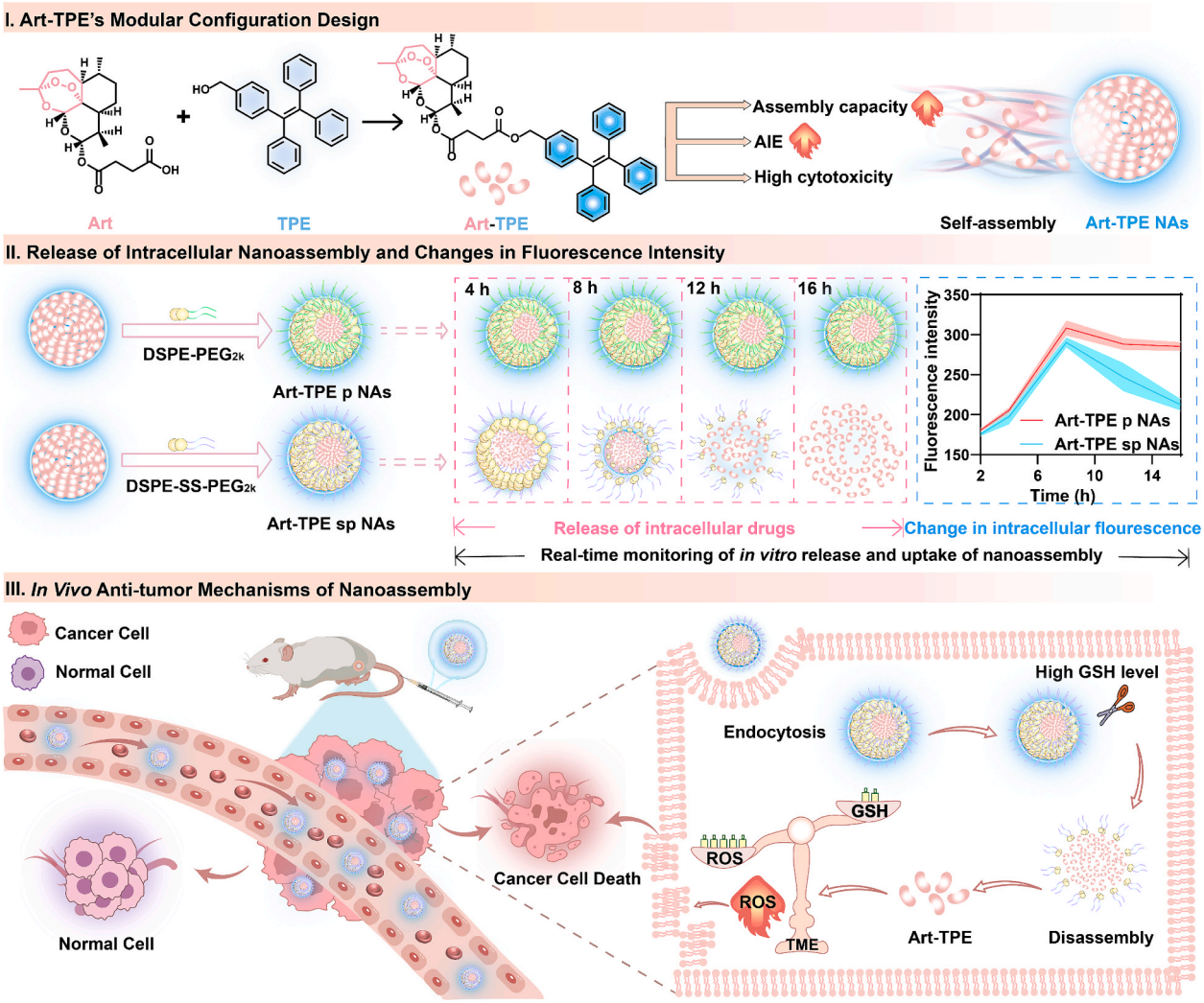

Fig. 1. Schematic representation of tumor therapeutic strategy employing Art-TPE NAs endowed with intracellular tracking functionality. I. Synthesis of Art-TPE and assembly procedure of Art-TPE NAs; II. The utilization of DSPE-PEG_{2K} and DSPE-SS-PEG_{2K} as PEG-based modifiers, a differentially engineered nano-tracker was prepared to monitor the release of intracellular NAs and the change of fluorescence intensity. III. *In vivo* anti-tumor mechanisms of NAs.

the yellow powdery product (Art-TPE) was purified *via* preparative liquid chromatography using an organic/aqueous phase ratio of 90:10 (v/v), yielding 62.5 % of the target compound. The resulting product was confirmed by mass spectrometry (FT-MS, solariX, Bruker, Germany) and nuclear magnetic resonance spectroscopy (600 MHz ^{1}H NMR, Bruker AV-400).

2.3. Preparation and characterization of Art-TPE NAs

The small-molecule self-assembled NAs were prepared *via* a one-step nanoprecipitation method. Specifically, Art-TPE (1 mg) was dissolved in tetrahydrofuran (THF)/absolute ethanol (1:1, v/v). The solution was then added dropwise to 1 mL of deionized water under continuous stirring (800 rpm) at room temperature. Subsequently, THF and ethanol were evaporated under reduced pressure at 25 °C, and the volume of Art-TPE NAs was supplemented to 1 mL. In addition, DSPE-PEG_{2K} (20 %, w/w) and DSPE-SS-PEG_{2K} (20 %, w/w) were added to Art-TPE NAs to prepare the Art-TPE p NAs and Art-TPE sp NAs. The particle size and zeta potential of the NAs were measured by the ZetaSizer (Nano ZS, Malvern Co., UK). The morphology of NAs was observed by a transmission electron microscope (TEM, Hitachi, HT7700, Japan) with 2 % phosphotungstic acid staining.

2.4. Exploration of the self-assembly mechanism

The molecular interactions governing the self-assembly of TPE NAs and Art-TPE NAs were systematically investigated through a dual-methodological approach. Initially, computational molecular docking simulations were performed using the AutoDock Vina software (version 1.2.3) to elucidate binding affinities and predominant interaction modes. Complementing these theoretical predictions, the presence of intermolecular forces in NAs was further verified *via* chemical destruction with sodium chloride (NaCl) for electrostatic screening, sodium dodecyl sulfate (SDS) for hydrophobic interaction disruption, and urea as a hydrogen-bond competitor. Briefly, TPE NAs and Art-TPE NAs were dispersed into NaCl, SDS, and urea at a concentration of 10 mM, and incubated at 37 °C thermostatically controlled shaking incubator (Noki, CHA-S, China) (100 rpm). At the predefined time points, the particle size changes of NAs were measured by the ZetaSizer.

2.5. In vitro colloidal stability

To assess the colloidal stability of Art-TPE NAs (1 mg/mL), Art-TPE p NAs (1 mg/mL), and Art-TPE sp NAs (1 mg/mL), the NAs were incubated in PBS (pH 7.4) and PBS (pH 7.4) supplemented with 10 % FBS at 37 °C in a thermostatically controlled shaking incubator. Fluorescence

intensity, average particle size, and zeta potential were measured periodically using a microplate reader (Thermo Scientific, H1M, USA) and ZetaSizer to monitor temporal changes. In addition to this, we also supplemented the storage stability of NAs (at 4 °C). Art-TPE NAs (1 mg/mL), Art-TPE p NAs (1 mg/mL), and Art-TPE sp NAs (1 mg/mL) were stored at 4 °C, and their particle size and zeta potential were measured on days 1, 2, 5, 7, 15, and 30 (n = 3).

2.6. Interpretation and mechanism validation of ACQ and AIE

The fluorescence intensity of the photosensitizer pyrodemagnesium chlorophyllin a (PPa), which exhibits an ACQ effect, was assessed in varying ratios of THF/aqueous solutions under 409 nm ultraviolet light irradiation. Fluorescence measurements were performed using a microplate reader with excitation and emission wavelengths set to 400 nm and 670 nm, respectively. Similarly, the fluorescence intensity of TPE was evaluated under identical experimental conditions [35]. Subsequently, the fluorescence behavior of Art-TPE was characterized with excitation at 320 nm and emission detection at 460 nm. The observed fluorescence enhancement was further validated through molecular dynamics simulations [36,37]. All geometric structures were optimized using the Gaussian 16 program package. The M06-2X hybrid functional was used for geometry optimization of the ground state and S1 excited state. While in ORCA 6.0.0, the TPSSh hybrid functional was used during TD-DFT calculations. The def2-SVP basis set was used during optimization, and the Def2-TZVP was used during fluorescence spectra. The solvent effect of THF was modeled using the polarizable continuum model during geometry optimization and single molecule detection during single-point calculations. The excitation properties were analysed by the Multiwfn software package 3.8 Dev and visualized by visual molecular dynamics (VMD). To further investigate the underlying molecular mechanisms, the average fluorescence lifetimes of TPE and Art-TPE were determined through fluorescence lifetime measurements, respectively. The calculation procedure is described as follows:

Fitting with a first-order exponential function, the average lifetime equation $\tau_{int} = B_1\tau_1^2/B_1\tau_1$.

Fitting with a second-order exponential function, the average lifetime equation $\tau_{int} = B_1\tau_1^2 + B_2\tau_2^2/B_1\tau_1 + B_2\tau_2$.

2.7. In vitro reduction-triggered disassembly of NAs

The reduction-stimulator dithiothreitol (DTT) was utilized to induce the disassembly of reduction-sensitive drugs, facilitating the investigation of changes in fluorescence intensity and particle size of Art-TPE sp NAs incubated with DTT at different concentrations (0, 5, 10, and 20 mM). The release study was conducted using PBS (pH 7.4) with 20 % absolute ethanol as the release medium. First, 1 mL of Art-TPE sp NAs (1 mg/mL) were placed in dialysis bags (MW = 8000–12000) and exposed to 29 mL of blank release media (0 mM DTT), as well as release media containing 5, 10, 20 mM DTT. Art-TPE sp NAs in the media were subsequently incubated at a thermostatically controlled shaking incubator (100 rpm). Samples of 200 μL of release medium were collected at 0, 2, 4, 6, and 8 h, with an equal volume of fresh release medium added back each time (n = 3). The cumulative release of Art-TPE sp NAs was determined by high-performance liquid chromatography (HPLC) (n = 3). The chromatographic conditions were as follows: a C18 column (4.6 × 250 mm, 5 μm), with a mobile phase of acetonitrile/water (100:0, v/v), a flow rate of 1.0 mL/min, and a detection wavelength of 214 nm.

2.8. Release and uptake of intracellular NAs

4T1 cells were seeded into 24-well plates at a density of 5×10^4 cells/well and incubated for 12 h. The medium was then aspirated and replaced with fresh medium containing Art-TPE p NAs and Art-TPE sp NAs, followed by incubation for 1, 2, 4, 8, 12, and 16 h (n = 3). After treatment, cells were washed three times with ice-cold PBS (pH 7.4) and fixed with 500 μL of 4 % paraformaldehyde (PFA). Release and uptake of intracellular NAs were visualized using confocal laser scanning microscopy (Nikon, *C*2, CLSM, Japan). To achieve precise intracellular localization, the cell membrane was labeled using DiR, followed by CLSM observation of nanotracer internalization. While maintaining identical cell densities and administration protocols as described previously, the experimental modifications were as follows: DiR was diluted in serum-free medium to a final working concentration of 1 μM. Subsequently, 15 μL of this solution was added per well and incubated for 30 min. Following incubation, cells were washed three times with ice-cold PBS (pH 7.4) and fixed with 500 μL of 4 % PFA. Intracellular NAs uptake dynamics were then visualized *via* CLSM at 1, 2, 4, 8, 12, and 16 h. In addition, for quantitative detection, the 4T1 cells were seeded into 12-well plates at a density of 2×10^5 cells/well for 1, 2, 4, 8, 12, and 16 h. Subsequently, cells were treated with the same method and washed, harvested, and suspended in PBS (pH 7.4) for analysis *via* FACS Calibur flow cytometer (FCM).

2.9. In vitro cytotoxicity assay

For cytotoxicity evaluation, the MTT assay was conducted. The 4T1 cells were cultured in RPMI 1640 culture medium supplemented with 1 % penicillin–streptomycin (100 μg/mL) and 10 % FBS in a cell incubator at 37 °C with 5 % CO_2. To assess biocompatibility, mouse NIH/3T3 murine embryonic fibroblast cells (3T3) were treated with the same formulations under identical experimental conditions (n = 3). The cytotoxicity of each group is calculated by the IC_{50} value. IC_{50} was calculated using the following formula:

$$\text{Cell viability} = (A_a - A_0)/(A_b - A_0) \times 100\ \%$$

The UV absorbance of the experimental, blank, and control groups was designated A_a, A_0, and A_b, respectively.

2.10. Cellular ROS detection

DCFH-DA was utilized to detect intracellular ROS levels. First, 4T1 cells were seeded into 24-well plates at a density of 5×10^4 cells/well and incubated at 37 °C and 5 % CO_2 for 12 h. Subsequently, the cells were treated with Art Sol, Art-TPE NAs, Art-TPE p NAs, and Art-TPE sp NAs (one control group was designated as the untreated cell cohort without any pharmacological intervention) (n = 3). After 4 h of incubation, cells were washed three times with ice-cold PBS (pH 7.4) and incubated with 10 μM DCFH-DA for 30 min. Following three additional washes with PBS (pH 7.4), the fluorescence intensity of DCF in the green channel was analyzed using CLSM. Additionally, the fluorescence intensity of ROS was quantified using FCM (n = 3).

In addition to intracellular ROS measurement, the antitumor efficacy was further validated through live/dead cell assays. While maintaining consistent cell densities and drug administration parameters as described previously, the experimental protocol was modified as follows: Dead cells were labeled with propidium iodide (PI, excitation: 488 nm, emission: 617 nm). The drug-containing medium was first removed, followed by washing the cells 3–4 times with ice-cold PBS (pH 7.4). Subsequently, sequential staining was performed by incubating the cells with 150 μL of PI staining solution, under light-protected conditions for 30 min. Unbound dyes were then removed through a final PBS (pH 7.4) wash. Proportion of dead cells was ultimately visualized *via* microplate reader and CLSM (n = 3).

2.11. Animal study

All animal procedures were performed in accordance with the Guidelines for Care and Use of Laboratory Animals of Shenyang Pharmaceutical University and approved by the Animal Ethics Committee of Shenyang Pharmaceutical University (No. SYPU-IACUC-2024–0311-

070).

2.12. Anti-tumor efficacy in vivo

A 4T1 tumor-bearing mouse model was established using female 11-week-old mice to evaluate the *in vivo* anti-tumor efficacy of the NAs. When the average tumor volume of mice reached approximately 100 mm^3, they were randomly divided into 6 groups: control group, Art Sol, Art-TPE Sol, Art-TPE NAs, Art-TPE p NAs, and Art-TPE sp NAs (n = 5). All formulations were administered *via* the tail vein every other day at an equivalent Art dose of 10 mg/kg for a total of five doses. Tumor volumes and body weights were measured every two days. Two days after the last treatment, blood samples were collected (The blood samples in collection tubes were centrifuged at 4000 rpm for 15 min, followed by supernatant collection), and major organs (heart, liver, spleen, lung, kidney) and tumors were harvested and fixed in 4 % PFA. The tumor was photographed, and the blood was centrifuged for hepatic and renal function analysis. The main organs and tumor tissues were stained with hematoxylin and eosin (H&E) staining for histopathology and TUNEL staining for apoptosis detection. To evaluate the long-term safety of NAs, a BALB/c female mouse model (body weight 20–22 g) was employed. Different concentrations of Art Sol (with high, medium, and low doses of 1, 0.5, and 0.25 mg/mL, respectively) and Art-TPE sp NAs (with high, medium, and low doses of 1, 0.5, and 0.25 mg/mL, respectively) were intravenously administered *via* the tail vein every other day for a total of four doses. Body weight changes and survival rates were monitored over a 40-day observation period.

2.13. Statistical analysis

All data were analyzed with GraphPad Prism and presented as mean ± standard deviation (SD). Significant differences between groups were assessed using either a T-test or a one-way analysis of variance (ANOVA). The exact *P* value is provided in the corresponding figure, with *P* values less than 0.05 considered statistically significant.

3. Results

3.1. Elaborate fabrication of nano-tracker

This project began with an interesting attempt to modularize the design of functional drugs (Fig. 2A), abandoning the traditional active-tumor-reactive chemical linker-assembly module for an active drug-functional assembly module (TPE), which greatly reduced the complexity of the synthesis reaction. Specifically, we successfully synthesized Art-TPE by the covalent attachment method (Figs. S1 and S2),

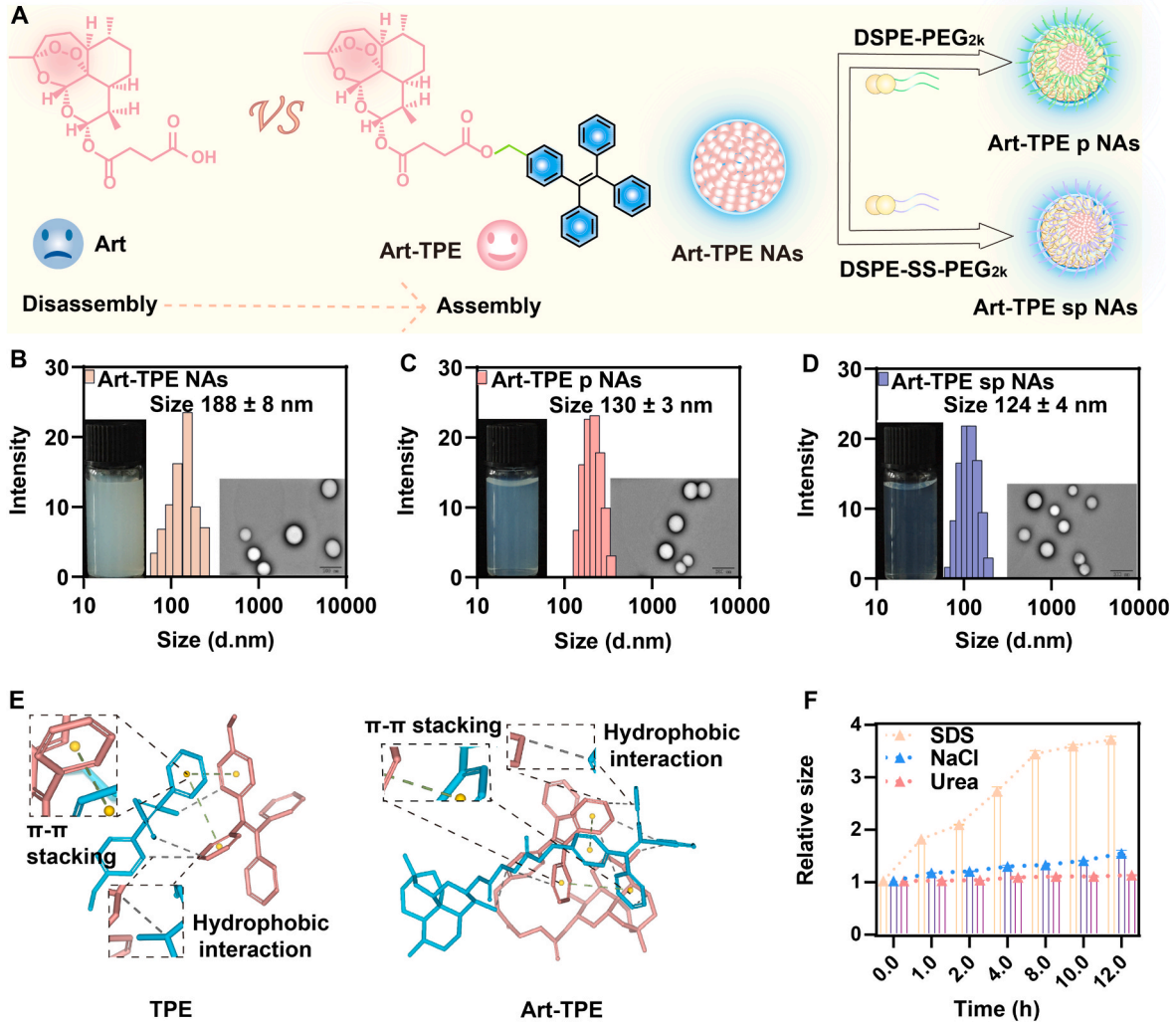

Fig. 2. Elaborate fabrication and characterization of NAs. (A) Enhancement of Art assembly capability *via* covalent conjugation with TPE and PEGylation modification of Art-TPE NAs. (B–D) TEM images and size distribution profiles of Art-TPE NAs, Art-TPE p NAs, and Art-TPE sp NAs. Scale bar = 200 nm. (E) Molecular docking simulation diagrams of TPE and Art-TPE NAs; (F) Changes in particle size of Art-TPE NAs treated with NaCl (10 mM), SDS (10 mM), and urea (10 mM). Data were presented as the mean ± SD (n = 3).

and proposed that the addition of TPE can not only promote molecular nanoassembly but also endow the Art-TPE with AIE properties. Interestingly, we found that Art-TPE had better assembly properties (particle size of 188 nm) compared to Art and TPE (Figs. S3 and S4, Fig. 2B). To improve colloidal stability and promote tumor-specific drug release, PEGylated NAs (Art-TPE sp NAs) were prepared by using DSPE-SS-PEG_{2K} containing disulfide bonds as release-activating module, and Art-TPE p NAs were prepared with DSPE-PEG_{2K} as surface modifiers, which were used as control groups. As shown in Fig. 2C–D, and Table S1, Art-TPE p NAs and Art-TPE sp NAs have very similar particle size distributions (~130 nm) and zeta potential (~ − 30 mV). We then investigated the mechanisms underlying Art-TPE NAs. Given the assembly driving force provided by TPE, we also studied the driving force of TPE NAs. Firstly, we explored the intermolecular forces using computer molecular docking techniques. As shown in Fig. 2E, two primary forces were identified as pivotal in the assembly process, including hydrophobic forces and π-π stacking interactions. Subsequently, we conducted additional experiments to validate the presence of these intermolecular forces through NAs destruction tests. As shown in Fig. 2F and Fig. S5, the particle size of NAs increased following incubation with SDS, indicating the predominance of hydrophobic interactions in nanoassembly. In contrast, no significant change in particle size occurred after separate incubation with NaCl or urea, indicating that electrostatic interactions and hydrogen bonding played secondary roles in molecular nanoassembly.

3.2. Investigation of the in vitro stability of NAs

The excellent nanoassembly properties are a prerequisite for the formation of NAs, but the stability of NAs is essential for achieving ideal delivery. To comprehensively evaluate the colloidal stability of NAs, systematic investigations were conducted on Art-TPE NAs, Art-TPE p NAs, and Art-TPE sp NAs (Fig. 3A). The three NAs were subjected to incubation in two distinct media: PBS (pH 7.4) and PBS (pH 7.4) containing FBS (10 %), simulating both simple physiological buffers and complex biological environments containing serum proteins. It was worth noting that Art-TPE p NAs and Art-TPE sp NAs showed good stability with negligibly changed fluorescence intensity, particle size, and zeta potential after incubation in PBS (pH 7.4) and PBS (pH 7.4) containing FBS (10 %) (Fig. 3C-D, Fig. 3F-I, Figs. S6 and S7), while the fluorescence intensity, particle size and zeta potential of non-PEGylated NAs (Art-TPE NAs) significantly changed under the same conditions (Fig. 3B and E, H-I, Figs. S6 and S7). In addition, we conducted storage stability test on the formulations at 4°C. The storage stability result demonstrated that the non-PEGylated NAs were unstable, with changes in particle size and zeta potential beginning to occur on the second day of storage, whereas the PEGylated NAs group exhibited consistent storage stability (Fig. S8 and S9). These results underscored the critical role of PEGylation in enhancing the colloidal stability of Art-TPE p NAs and Art-TPE sp NAs.

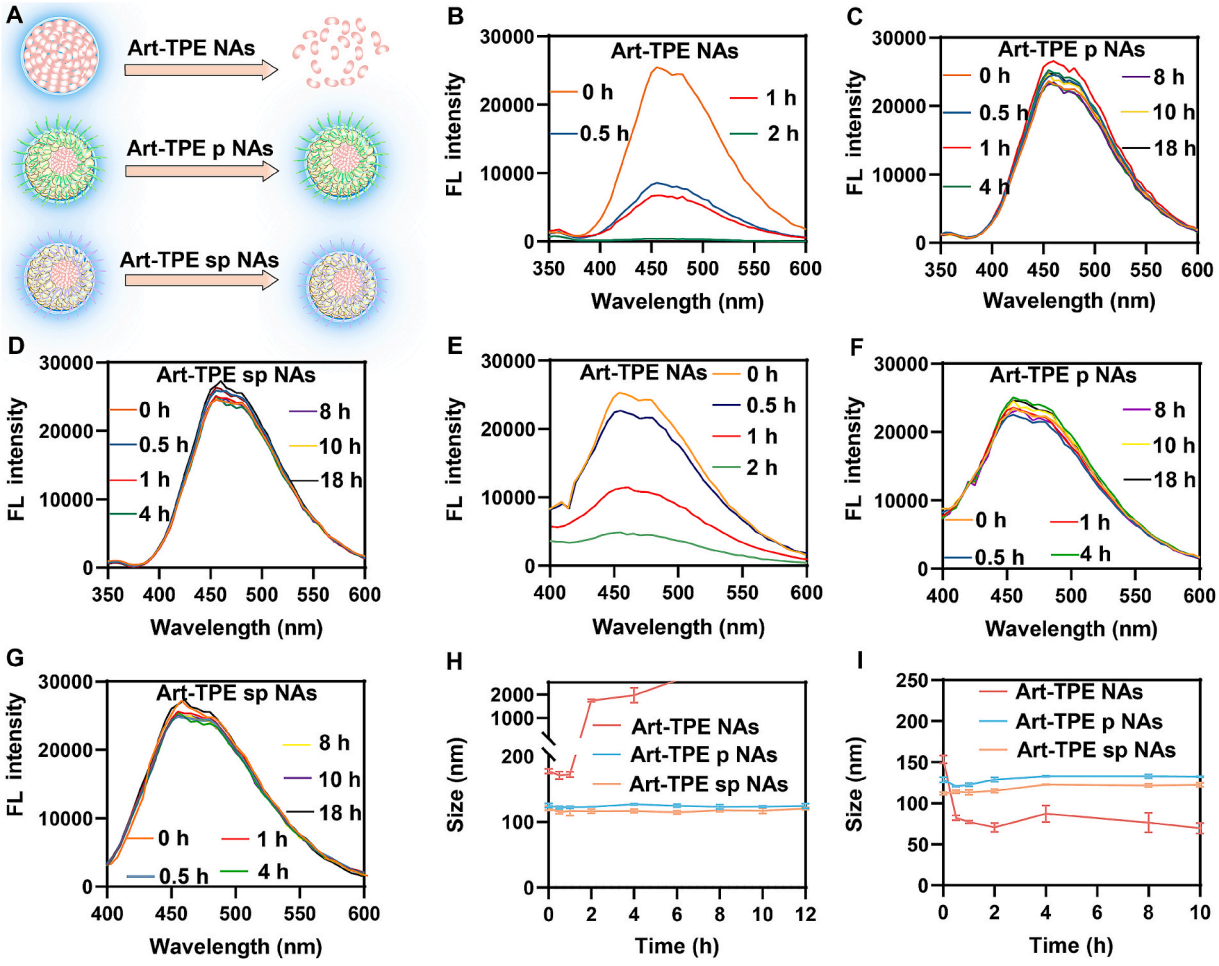

Fig. 3. Investigation of the *in vitro* stability of NAs. (A) Schematic diagram of Art-TPE NAs, Art-TPE p NAs, and Art-TPE sp NAs treated with PBS (pH 7.4) and PBS (pH 7.4) with 10 % FBS. (B–D) Changes in fluorescence intensity of Art-TPE NAs, Art-TPE p NAs, and Art-TPE sp NAs in PBS (pH 7.4). (E–G) Changes in fluorescence intensity of Art-TPE NAs, Art-TPE p NAs, Art-TPE sp NAs with 10 % FBS (pH 7.4). (H-I) Particle size changes of NAs in PBS (pH 7.4) and PBS (pH 7.4) containing 10 % FBS. Data of H and I were presented as the mean ± SD (n = 3).

3.3. Advantages of AIEgens and verification of its luminescence principle

Firstly, we systematically compared the fluorescence behavior of the organic fluorescent dye PPa with the ACQ phenomenon and the classical AIE luminophore TPE in different solvent environments. As shown in Fig. 4A, PPa exhibited a high fluorescence intensity in THF solution, but the fluorescence intensity decreased as the moisture content in the solvent increased. This was due to the low solubility of PPa in water, the easy aggregation between molecules, and the increase of non-radiative transitions, which severely limited its performance in high-brightness fluorescence applications. In contrast, TPE could rotate freely around a single bond in THF (a good solvent), consuming excited-state energy *via* non-radiative transitions and resulting in weak fluorescence. However, as the solvent environment gradually changed from good to poor, the intramolecular rotation was restricted, leading to enhanced fluorescence (Fig. 4B).

To test our hypothesis, the same method was used to investigate the AIE properties of Art-TPE. As shown in Fig. 4C, the AIE performance of Art-TPE was significantly enhanced compared with that of TPE, which may be attributed to the further intensification of the RIM effect of Art structure on TPE molecules during aggregation, thereby increasing their fluorescence intensity. To further explore the enhancement mechanism, quantum chemical calculations were used to analyze the energy level transition characteristics of TPE and Art-TPE. The results showed that at specific wavelengths, the molar absorbance coefficient and oscillation intensity of Art-TPE were significantly higher than that of TPE (Fig. 4D–E), which significantly improved the photon absorption capacity of Art-TPE and enhanced the fluorescence intensity. Overall, integrating TPE and the covalent Art-conjugation strategy not only enhanced Art's self-assembly capability but also endowed Art-TPE NAs with intrinsic fluorescence, enabling real-time cellular tracking of NAs. Furthermore, the measured average fluorescence lifetimes demonstrated distinct values of 4.6 ns for TPE and 5.9 ns for Art-TPE (Fig. 4F–G, Tables S2–S5). This result was consistent with the previous fluorescence intensity results and provided support for the increase of fluorescence intensity.

3.4. Disintegration of NAs in vitro

While the nanoassembly properties and stability of NAs are critical for efficient delivery, tumor-specific delivery is essential to achieve effective intracellular drug tracking and anti-tumor efficacy. As

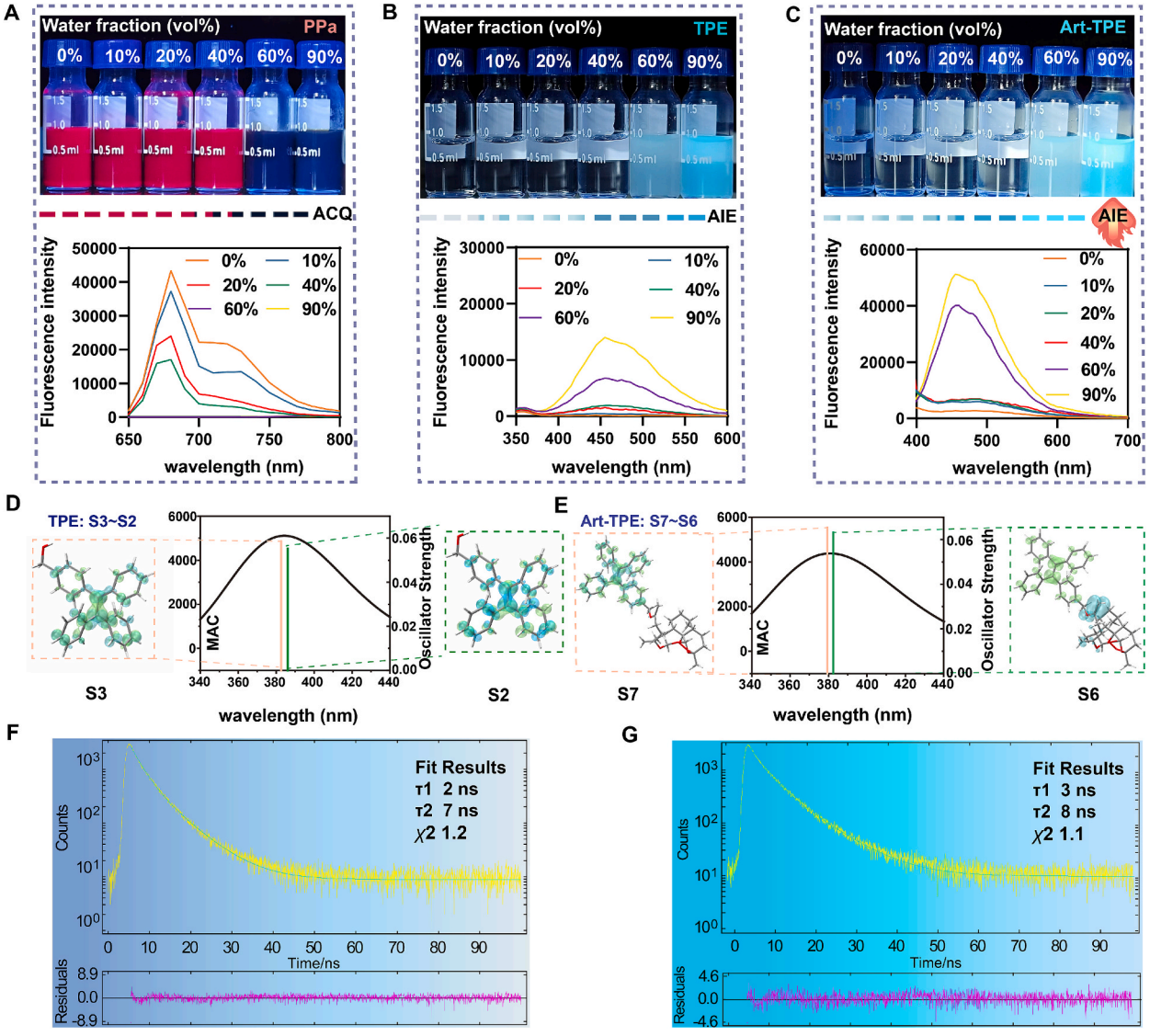

Fig. 4. The verification of luminescence principle. (A) Changes in the fluorescence of PPa in solvents with different water contents. (B) Changes in the fluorescence of TPE in solvents with different water contents. (C) Changes in the fluorescence of Art-TPE in solvents with different water contents. (D–E) The energy level transitions of TPE and Art-TPE were calculated by quantum chemistry (MAC: Molar absorption coefficient). (F-G) The fluorescence lifetime measurements of TPE and Art-TPE.

previously mentioned, DSPE-SS-PEG_{2K} containing disulfide bonds was used to prepare reduction-responsive NAs. To assess their redox responsiveness, we investigated the changes of fluorescence intensity, particle size, and drug release of NAs upon varying concentrations of DTT (Fig. 5A). As shown in Fig. 5B-G, the fluorescence intensity and particle size of Art-TPE sp NAs changed significantly upon exposure to 5, 10, and 20 mM DTT compared to the blank medium (0 mM DTT). In addition, it showed time- and DTT concentration-dependent release. On the contrary, given that there were no reduction- sensitive bonds in Art-TPE p NAs, the changes of fluorescence intensity and particle size in the presence of DTT were negligible (Figs. S10 and S11). In addition to the changes of fluorescence intensity and particle size, we systematically analyzed the release behavior of Art-TPE sp NAs at different concentrations of DTT (0, 5, 10, 20 mM DTT) (Fig. 5H). The release profiles demonstrated that cumulative release under 0 mM DTT plateaued at 15.2 % after 4 h, with no subsequent increase. In contrast, cumulative release at 4 h exhibited a progressive increase at concentrations of 5, 10, and 20 mM DTT. Significantly, the 20 mM DTT group achieved 78.3 % cumulative release at 4 h, peaked at 81.6 % by 6 h, followed by a plateau phase in the release curve. These results indicated that the DSPE-SS-PEG_{2K} modified Art-TPE sp NAs had the characteristics of reduction-responsive release, which had the potential to achieve specific release within tumor cells.

3.5. Tracing the intracellular fate of NAs

Leveraging the intrinsic AIE fluorescence properties of Art-TPE NAs, the cellular uptake and intracellular release characteristics were investigated by comparing fluorescence intensity variations between two PEGylated NAs. As shown in Fig. 6B–C, Figs. S12 and S13, the results demonstrated that both NAs exhibited a gradual increase in fluorescence intensity within the initial 8 h, indicating time-dependent cellular uptake, which suggested a higher uptake rate relative to the release rate. However, beyond 8 h, the fluorescence intensity of Art-TPE p NAs remained stable, whereas that of Art-TPE sp NAs declined, exhibiting gradual reduced fluorescence intensity to 16 h. These findings imply that both NAs reached peak cellular uptake at 8 h. Notably, the post-8 h fluorescence divergence arose from disassembly and release of Art-TPE sp NAs, leading to attenuation of AIE and subsequent fluorescence reduction.

3.6. In vitro cytotoxicity and ROS evaluation

Given the favorable anti-tumor activity of Art, the MTT assay was used to investigate the cytotoxicity of NAs in 4T1 cells. As shown in Fig. 6D, the cytotoxicity of TPE Sol at the concentration of 0.2–5 μM was negligible, and Art-TPE Sol exhibited cytotoxicity comparable to Art Sol, confirming that the introduction of TPE did not affect the activity of Art. In contrast, Art Sol and Art-TPE Sol exhibited poor cytotoxicity, which could be due to their poor cellular uptake capacity (Fig. 6D). In addition, due to the poor colloidal stability of Art-TPE NAs, there was no significant increase in cytotoxicity compared to Art-TPE Sol (Fig. 6D). Compared with Art-TPE Sol, Art-TPE p NAs and Art-TPE sp NAs showed stronger cytotoxicity due to good cellular uptake (Fig. 6D). The

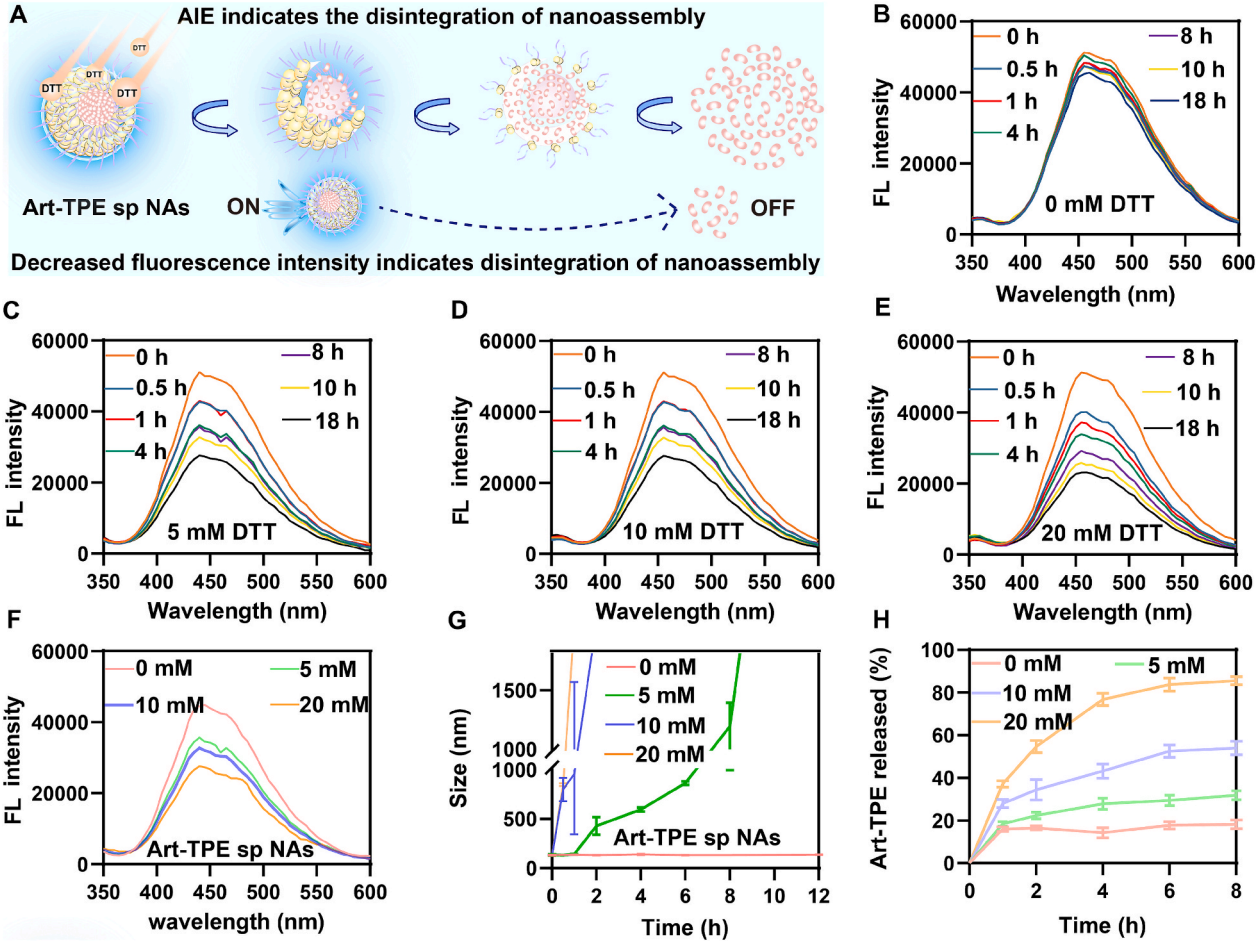

Fig. 5. Disintegration of NAs *in vitro*. (A) Schematic diagram of the simulated release of Art-TPE sp NAs at the tumor site. (B–F) Fluorescence changes of Art-TPE sp NAs in the presence of DTT (0, 5, 10, and 20 mM DTT). (G) Particle size changes of Art-TPE sp NAs in the presence of DTT (0, 5, 10, and 20 mM DTT) (n = 3). (H) Release of Art-TPE sp NAs by HPLC at 0, 5, 10, and 20 mM DTT (n = 3). Data of G-H were presented as the mean ± SD (n = 3).

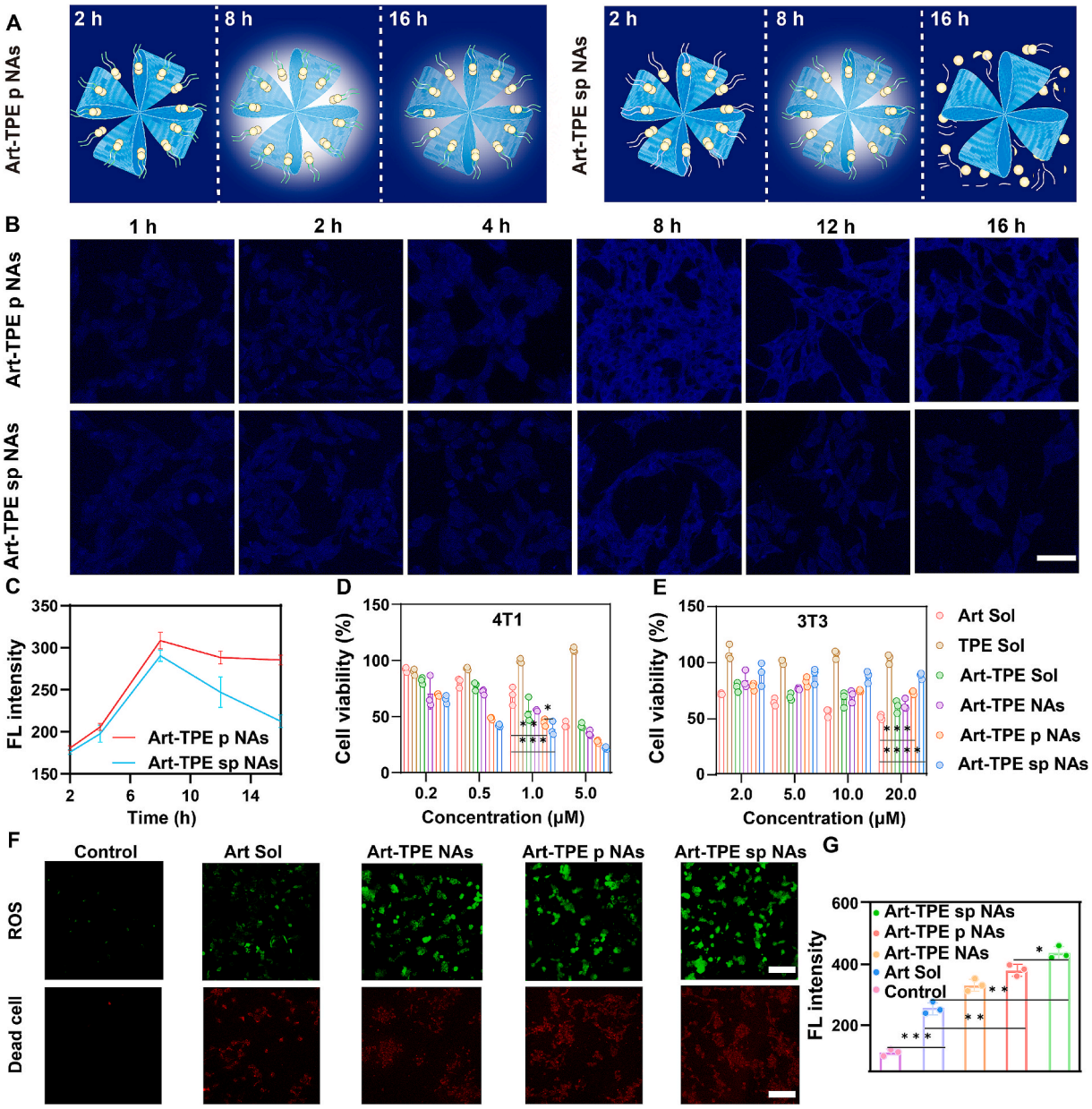

Fig. 6. Insight into intracellular fate and mechanism. (A) Schematic illustration of intracellular fluorescence changes in Art-TPE p NAs and Art-TPE sp NAs. (B–C) CLSM qualitative images and FCM quantitative analysis (n = 3) of intracellular fate in 4T1 cells at different time points. Scale bar = 50 μm. (D-E) In vitro cytotoxicity of 4T1 cells and 3 T3 cells treated with different formulations (n = 3). (F) CLSM images of intracellular ROS and dead cells in 4T1 cells after treatment. Scale bar = 100 μm. (G). FCM quantitative analysis (n = 3) of intracellular ROS levels in 4T1 cells after treatment. Data of C-E and G were presented as the mean ± SD (n = 3). *p < 0.05, **p < 0.01, ***p < 0.001, and ****p < 0.0001.

enhanced cytotoxicity of Art-TPE sp NAs might be attributed to their effective uptake and rapid release in cells with reductive reactivity. In addition, compared with Art Sol and Art-TPE Sol, Art-TPE p NAs and Art-TPE sp NAs showed negligible cytotoxicity to 3T3 cells, indicating good biocompatibility of NAs(Fig. 6E). Overall, Art-TPE sp NAs not only exhibited good anti-tumor effect, but also provided good therapeutic selectivity through tumor-specific nanostructure disassembly.

The anti-tumor efficacy of Art primarily stems from the peroxide bridge within its molecular structure. This distinctive moiety reacts with intracellular ferrous iron, triggering the cleavage of the peroxide bridge and generating carbon-centered free radicals or ROS. Based on this, intracellular ROS levels after treatment with Art Sol, Art-TPE NAs, Art-TPE p NAs, and Art-TPE sp NAs were validated using CLSM and FCM. As shown in Fig. 6F-G, Art-TPE sp NAs produced more ROS than Art Sol, resulting in tumor cell death. These results indicated improvements in precisely prepared NAs are associated with enhanced anti-tumor efficacy. In addition to intracellular ROS detection, the antitumor efficacy was further validated through live/dead cell viability assays. As demonstrated in Fig. 6F and Fig. S14, Art-TPE sp NAs-treated 4T1 cells exhibited an increased proportion of dead cells, correlating with anti-tumor activity.

3.7. *Anti-tumor activity in vivo*

To investigate the anti-tumor activity *in vivo*, a 4T1 breast tumor mouse model was established. Saline, Art Sol, Art-TPE Sol, Art-TPE NAs, Art-TPE p NAs, and Art-TPE sp NAs were administered intravenously to tumor-bearing mice every other day for a total of five intravenous injections (Fig. 7A). Two days after the final injection, the major organs as well as tumors were harvested to evaluate therapeutic effects. As shown

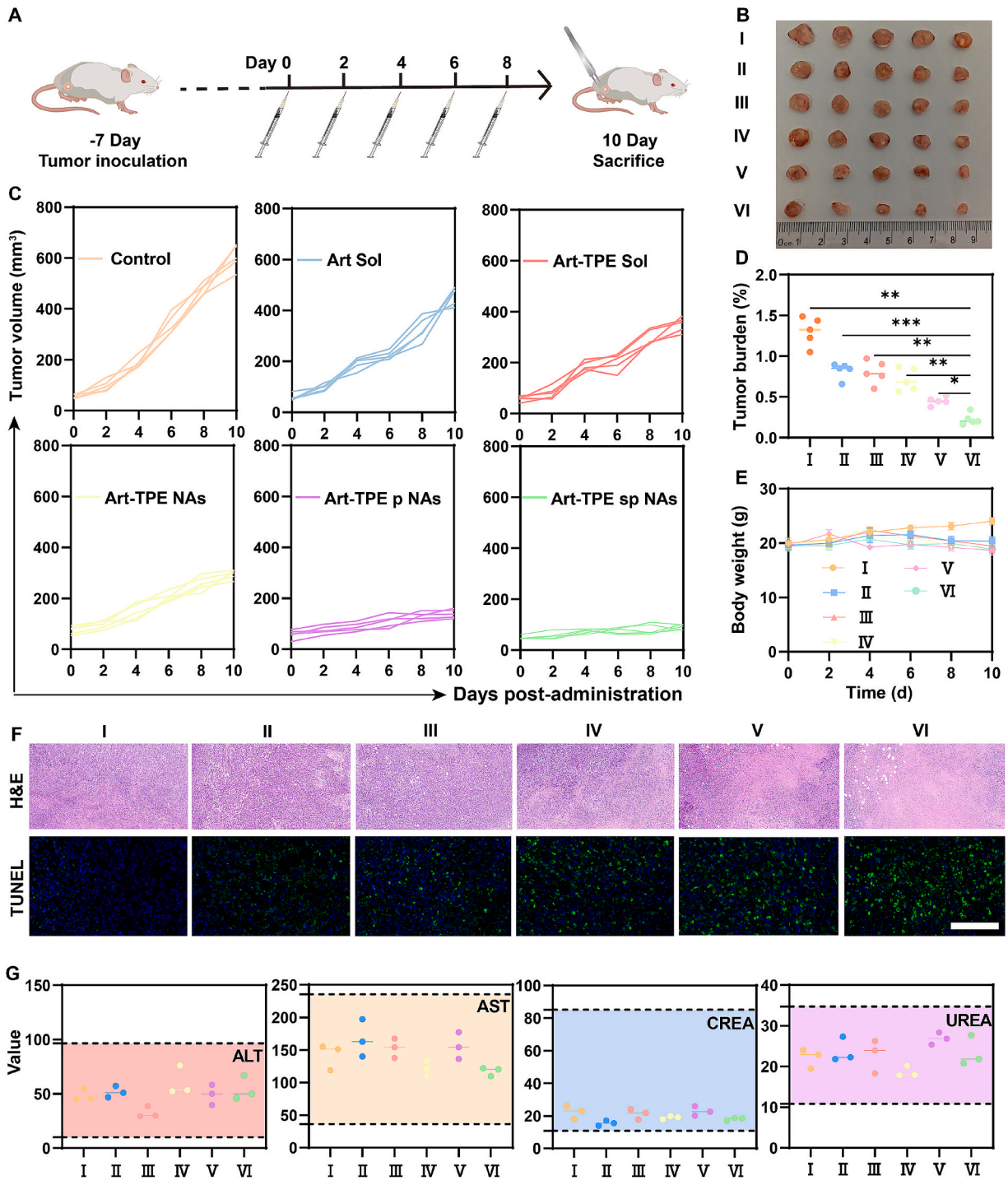

Fig. 7. *In vivo* anti-tumor activity. (A) Schematic illustration of the treatment schedule. (B) Images of tumors after the last treatment (n = 5). (C) Tumor growth curves of 4T1 tumor-bearing mice receiving different treatments (n = 5). (D) Tumor burden in 4T1 tumor-bearing mice after different treatments (n = 5). (E) Change in body weight during treatment (n = 5). Data of C-E were presented as the mean ± SD (n = 5). (F) H&E and TUNEL staining images of tumors after various treatments. Scale bar = 100 μm. (G) Hepatic and renal function indicators of mice-bearing tumor after the last treatment (n = 3). Data of G were presented as the mean ± SD (n = 3). I. Control, II. Art Sol, III. Art-TPE Sol, IV. Art-TPE NAs, V. Art-TPE p NAs, VI. Art-TPE sp NAs. *p < 0.05, **p < 0.01, and ***p < 0.001.

in Fig. 7B-D, Art Sol, TPE Sol, and Art-TPE Sol exhibited poor anti-tumor effects, mainly due to their rapid clearance after intravenous injection. Similarly, Art-TPE NAs showed limited inhibitory effect on tumors due to their instability (Fig. 7B–D). On the contrary, Art-TPE p NAs and Art-TPE sp NAs exhibited significant tumor suppressive effects (Fig. 7B–D). Notably, Art-TPE sp NAs exhibited optimal tumor suppression effects due to their reactive release at the tumor site (Fig. 7B–D). In addition, TUNEL and H&E staining results correlated with tumor suppression outcomes, further supporting the antitumor efficacy of Art-TPE sp NAs (Fig. 7F). Finally, the *in vivo* safety profile of Art-TPE NAs was characterized. As shown in Fig. 7E and G, and Fig. S15, multiple treatments did not lead to significant abnormalities in body weight and hepatorenal function parameters, with no organ damage observed. Long-term toxicity experiments examined the weight changes and survival curves of mice at different doses of NAs. The results showed that Art Sol had a significant decrease in weight at medium and high doses, and a slight

increase in weight at different doses of Art-TPE sp NAs, indicating that Art Sol might have potential toxicity when the dose reached a certain concentration, while Art-TPE sp NAs did not show potential toxicity under the same conditions (Fig. S16). In addition, the survival rate curve also confirmed (Fig. S17).

4. Conclusion

In summary, we designed differentiated nanotrackers with promising antitumor activity for investigating intracellular drug uptake and release. Conventional nano-delivery systems often require efficient drug delivery through carriers [38], and small molecule prodrug self-assembly technology usually consists of three parts: assembly module, response module, and treatment module [39]. Differently, the carrier-free NAs we designed directly coupled Art to TPE, discarding the response module, reducing the difficulty of synthesis and maintaining effective antitumor activity. Moreover, the cellular uptake and release mechanisms of traditional tumor-responsive nanomedicines are not well understood [40]. In this project, TPE molecule with AIE properties were introduced as functional side chains, which not only endowed antitumor nanodrugs with luminescence properties but also unexpectedly discovered their fluorescence enhancement after synthesis. For further optimization, we chose DEPE-SS-PEG_{2k} as a response module to modify in NAs to enhance the stability of NAs during systemic circulation and promote disulfide bond cleavage in the redox tumor microenvironment, thereby enabling tumor-specific drug release and synchronous fluorescence signal feedback. The effective anti-tumor efficacy of Art-TPE has been further validated in a 4T1 tumor-bearing mouse model, highlighting its therapeutic potential. This bifunctional nanotracker not only provides a new paradigm for the effective antitumor therapy of small-molecule self-assembled nanomedicines, but also establishes a good platform for real-time imaging of intracellular drug uptake and release.

In the future, we hope to combine advanced materials with excellent anti-tumor drugs and nano-delivery technology to achieve the integration of diagnosis and treatment and amplify the efficacy. The TPE derivative Art-TPE exhibited a short emission wavelength, which intrinsically limited its tissue penetration capacity, thereby restricting its application in real-time monitoring for *in vivo* imaging modalities. Future efforts are anticipated to focus on selecting AIE groups with longer wavelengths and linking them with drugs to achieve real-time visualization in both *in vitro* and *in vivo* therapy.

CRediT authorship contribution statement

MiriGuli Musa: Writing – original draft, Project administration, Methodology, Formal analysis, Data curation, Conceptualization. **Xinxin Sun:** Writing – review & editing, Project administration, Methodology, Formal analysis, Data curation, Conceptualization. **Jianbin Shi:** Writing – review & editing, Methodology, Formal analysis. **Jing Li:** Writing – review & editing, Resources. **Shenwu Zhang:** Writing – review & editing, Resources, Methodology, Formal analysis, Data curation, Conceptualization. **Xianbao Shi:** Writing – review & editing, Resources, Methodology, Funding acquisition, Formal analysis, Data curation, Conceptualization.

Declaration of competing interest

The authors declare that they have no known competing financial interests or personal relationships that could have appeared to influence the work reported in this paper.

Acknowledgments

This work was financially supported by the Application Basic Research Project of Liaoning Provincial Department of Science and Technology (2023JH2/101700072).

Appendix A. Supplementary data

Supplementary data to this article can be found online at https://doi.org/10.1016/j.jcis.2025.138199.

Data availability

The authors do not have permission to share data.

References

[1] M. Saha, S.S. Ghosh, Engineered hybrid nanosystem for homologous targeting of EMT induced triple negative breast cancer cells, ACS Appl. Bio Mater. 6 (2) (2023) 681–693, https://doi.org/10.1021/acsabm.2c00925.
[2] T. Al-Batsh, A.-R. Nayef, A.-M. Yosra, E.-K. Osama, S. Baha, T. Faris, H. Abdel-Razeq, Escalation and de-escalation strategies for endocrine therapy in early-stage breast cancer, Biologics Targets Ther. 19 (2025) 97–111, https://doi.org/10.2147/btt.s508634.
[3] E. Agostinetto, J. Gligorov, M. Piccart, Systemic therapy for early-stage breast cancer: learning from the past to build the future, Nat. Rev. Clin. Oncol. 19 (12) (2022) 763–774, https://doi.org/10.1038/s41571-022-00687-1.
[4] L. Wilkinson, T. Gathani, Understanding breast cancer as a global health concern, Br. J. Radiol. 95 (1130) (2021), https://doi.org/10.1259/bjr.20211033.
[5] F. Wu, X. An, S. Li, C. Qiu, Y. Zhu, Z. Ye, S. Song, Y. Wang, D. Shen, X. Di, Y. Yao, W. Zhu, X. Jiang, X. Shi, R. Chen, L. Kou, Enhancing chemoimmunotherapy for colorectal cancer with paclitaxel and alantolactone *via* CD44-Targeted nanoparticles: a STAT3 signaling pathway modulation approach, Asian J. Pharm. Sci. 20 (1) (2025) 100993, https://doi.org/10.1016/j.ajps.2024.100993.
[6] N. Ito, N. Ahmed, U. Koichiro, M. Ebara, Poly (ARTEMA), a novel artesunate-based polymer induces ferroptosis in breast cancer cells, Sci. Technol. Adv. Mater. 26 (1) (2025) 2482514, https://doi.org/10.1080/14686996.2025.2482514.
[7] A.L. Greenshields, W. Fernando, D.W. Hoskin, The anti-malarial drug artesunate causes cell cycle arrest and apoptosis of triple-negative MDA-MB-468 and HER2-enriched SK-BR-3 breast cancer cells, Exp. Mol. Pathol. 107 (2019) 10–22, https://doi.org/10.1016/j.yexmp.2019.01.006.
[8] B. Dupouy, L. Cotos, A. Binder, L. Slavikova, M. Rottmann, P. Mäser, D. Jacquemin, M. Ganter, E. Davioud-Charvet, M. Elhabiri, Click coupling of flavylium dyes with plasmodione analogues: towards new redox-sensitive pro-fluorophores, Chem. Eur. J. 31 (6) (2025) e202403691, https://doi.org/10.1002/chem.202403691.
[9] M. Gomes, I. Ribeiro, M. Warsame, H. Karunajeewa, M. Petzold, Rectal artemisinins for malaria: a review of efficacy and safety from individual patient data in clinical studies, BMC Infect. Dis. 8 (1) (2008) 39, https://doi.org/10.1186/1471-2334-8-39.
[10] A. Speciale, C. Muscarà, M.S. Molonia, M. Cristani, F. Cimino, A. Saija, Recent advances in glycyrrhetinic acid-functionalized biomaterials for liver cancer-targeting therapy, Molecules 27 (6) (2022) 1775, https://doi.org/10.3390/molecules27061775.
[11] P.S. Twomey, B.L. Smith, C. McDermott, A. Novitt-Moreno, W. McCarthy, S. P. Kachur, P.M. Arguin, Intravenous artesunate for the treatment of severe and complicated malaria in the United States: clinical use under an investigational new drug protocol, Ann. Intern. Med. 163 (7) (2015) 498–506, https://doi.org/10.7326/m15-0910.
[12] P. Couvreur, S. Lepetre-Mouelhi, E. Garbayo, M.J. Blanco-Prieto, Self-assembled lipid–prodrug nanoparticles, Nat. Rev. Bioeng. 1 (10) (2023) 749–768, https://doi.org/10.1038/s44222-023-00082-0.
[13] M.A. Campea, A. Lofts, F. Xu, M. Yeganeh, M. Kostashuk, T. Hoare, Disulfide-cross-linked nanogel-based nanoassemblies for chemotherapeutic drug delivery, ACS Appl. Mater. Interfaces 15 (21) (2023) 25324–25338, https://doi.org/10.1021/acsami.3c02575.
[14] R. Liu, C. Luo, Z. Pang, J. Zhang, S. Ruan, M. Wu, L. Wang, T. Sun, N. Li, L. Han, J. Shi, Y. Huang, W. Guo, S. Peng, W. Zhou, H. Gao, Advances of nanoparticles as drug delivery systems for disease diagnosis and treatment, Chin. Chem. Lett. 34 (2) (2023) 107518, https://doi.org/10.1016/j.cclet.2022.05.032.
[15] S.K. Misra, Z. Wu, F. Ostadhossein, M. Ye, K. Boateng, K. Schulten, E. Tajkhorshid, D. Pan, Pro-nifuroxazide self-assembly leads to triggerable nanomedicine for anti-cancer therapy, ACS Appl. Mater. Interfaces 11 (20) (2019) 18074–18089, https://doi.org/10.1021/acsami.9b01343.
[16] B.S. Shivaji, R. Boddula, A. Saeki, S.P. Singh, A phenothiazine-fused electroactive bilayer helicene: design, synthesis, ACQ-to-AIE transformation and photophysical properties, J. Mater. Chem. C 10 (13) (2022) 5173–5182, https://doi.org/10.1039/d1tc06090b.
[17] R.T. Kwok, C.W. Leung, J.W. Lam, B.Z. Tang, Biosensing by luminogens with aggregation-induced emission characteristics, Chem. Soc. Rev. 44 (13) (2015) 4228–4238, https://doi.org/10.1039/c4cs00325j.
[18] C.F.A. Gomez-Duran, R. Hu, G. Feng, T. Li, F. Bu, M. Arseneault, B. Liu, E. Peña-Cabrera, B.Z. Tang, Effect of AIE substituents on the fluorescence of tetraphenylethene-containing BODIPY derivatives, ACS Appl. Mater. Interfaces 7 (28) (2015) 15168–15176, https://doi.org/10.1021/acsami.5b05033.
[19] F. Würthner, Aggregation-induced emission (AIE): a historical perspective, Angew. Chem. Int. Ed. 59 (34) (2020) 14192–14196, https://doi.org/10.1002/anie.202007525.

[20] A.C.B. Rodrigues, J.S.S. de Melo, Aggregation-induced emission: from small molecules to polymers—historical background, mechanisms and photophysics, Springer Cham., (2022) pp. 209-246, DOI: 10.1007/s41061-021-00327-9.
[21] M.A. Pantelaiou, D. Vagenas, E.S. Karvelis, G. Rotas, S. Pispas, Co-assembled nanosystems exhibiting intrinsic fluorescence by complexation of amino terpolymer and its quaternized analog with Aggregation-induced emission (AIE) dye, Nanomaterials 14 (20) (2024) 1631, https://doi.org/10.3390/nano14201631.
[22] P. Ramezani, S.C. De Smedt, F. Sauvage, Supramolecular dye nanoassemblies for advanced diagnostics and therapies, Bioeng. Transl. Med. 9 (4) (2024) e10652, https://doi.org/10.1002/btm2.10652.
[23] K. Saczuk, M. Dudek, K. Matczyszyn, M. Deiana, Advancements in molecular disassembly of optical probes: a paradigm shift in sensing, bioimaging, and therapeutics, Nanoscale Horiz. 9 (9) (2024) 1390–1416, https://doi.org/10.1039/d4nh00186a.
[24] S. Kansız, Y.M. Elçin, Advanced liposome and polymersome-based drug delivery systems: considerations for physicochemical properties, targeting strategies and stimuli-sensitive approaches, Adv. Colloid Interface Sci. 317 (2023) 102930, https://doi.org/10.1016/j.cis.2023.102930.
[25] S. Suzuki, S. Sasaki, A.S. Sairi, R. Iwai, B.Z. Tang, G.-I. Konishi, Principles of aggregation-induced emission: design of deactivation pathways for advanced AIEgens and applications, Angew. Chem. Int. Ed. 59 (25) (2020) 9856–9867, https://doi.org/10.1002/anie.202000940.
[26] D.D. La, S.V. Bhosale, L.A. Jones, S.V. Bhosale, Tetraphenylethylene-based AIE-active probes for sensing applications, ACS Appl. Mater. Interfaces 10 (15) (2018) 12189–12216, https://doi.org/10.1021/acsami.7b12320.
[27] A. Walker Leah, J. Sullivan David, Impact of extended duration of artesunate treatment on parasitological outcome in a cytocidal murine malaria model, Antimicrob. Agents Chemother. 61 (4) (2017), https://doi.org/10.1128/aac.02499-16.
[28] P. Khanal, Antimalarial and anticancer properties of artesunate and other artemisinins: current development, Monatsh. Chem. 152 (4) (2021) 387–400, https://doi.org/10.1007/s00706-021-02759-x.
[29] D. Varadharajan, H. Turgut, J. Lahann, H. Yabu, G. Delaittre, Surface-reactive patchy nanoparticles and nanodiscs prepared by tandem nanoprecipitation and internal phase separation, Adv. Funct. Mater. 28 (39) (2018) 1800846, https://doi.org/10.1002/adfm.201800846.
[30] K.P. Adzavon, W. Zhao, X. He, W. Sheng, Ferroptosis resistance in cancer cells: nanoparticles for combination therapy as a solution, Front. Pharmacol. 15 (2024) 1416382, https://doi.org/10.1016/j.cis.2023.102930.
[31] K. Roy, D.-H. Lee, B. Ryplida, I. In, S.H. Bhang, S.Y. Park, A self-reporting mineralized conductive hydrogel sensor with cancer-selective viscosity, adhesiveness, and stretchability, Adv. Funct. Mater. 33 (16) (2023) 2212977, https://doi.org/10.1002/adfm.202212977.
[32] L. Gallego-Yerga, C. de la Torre, F. Sansone, A. Casnati, C.O. Mellet, J.M. García Fernández, V. Ceña, Synthesis, self-assembly and anticancer drug encapsulation and delivery properties of cyclodextrin-based giant amphiphiles, Carbohydr. Polym. 252 (2021) 117135, https://doi.org/10.1016/j.carbpol.2020.117135.
[33] B. Ma, Y. Nishina, A. Bianco, A glutathione responsive nanoplatform made of reduced graphene oxide and MnO_2 nanoparticles for photothermal and chemodynamic combined therapy, Carbon 178 (2021) 783–791, https://doi.org/10.1016/j.carbon.2021.03.065.
[34] A. Domiński, T. Konieczny, K. Duale, M. Krawczyk, G. Pastuch-Gawołek, P. Kurcok, Stimuli-responsive aliphatic polycarbonate nanocarriers for tumor-targeted drug delivery, Polymers 12 (12) (2020) 2890, https://doi.org/10.3390/polym12122890.
[35] Y. Mise, K. Imato, T. Ogi, N. Tsunoji, Y. Ooyama, Fluorescence sensors for detection of water based on tetraphenylethene–anthracene possessing both solvatofluorochromic properties and aggregation-induced emission (AIE) characteristics, New J. Chem. 45 (9) (2021) 4164–4173, https://doi.org/10.1039/dinj00186h.
[36] D.K. Sivadas, P. Gayathri, S. Ravi, S. Karthikeyan, M. Pannipara, A.G. Al-Sehemi, D. Moon, S.P. Anthony, V. Madhu, Distinct fluorescence state, mechanofluorochromism of terpyridine conjugated fluorophores and the reusable sensing of nitroaromatics in aqueous medium, New J. Chem. 47 (27) (2023) 12770–12778, https://doi.org/10.1039/d3nj01235b.
[37] A. Sánchez-Ruiz, A. Sousa-Hervés, J. Tolosa Barrilero, A. Navarro, J.C. Garcia-Martinez, Aggregation-induced emission properties in fully π-conjugated polymers, dendrimers, and oligomers, Polymers 13 (2) (2021) 213, https://doi.org/10.3390/polym13020213.
[38] J.A. Malik, A.J. Ajgar, A. Sakeel, K. Afreen, A. Nafees, S. Anwar, Nano-drug delivery system: a promising approach against breast cancer, Ther. Deliv. 14 (5) (2023) 357–381, https://doi.org/10.4155/tde-2023-0020.
[39] W. Wang, S. Wang, S. Xu, R. Chai, J. Yuan, H. Zhang, Y. Li, X. Pu, X. Li, J. Sun, The assembly modules deformation strategy improved the chemical stability and self-assembly stability of docetaxel prodrugs nanoassemblies, Nanoscale 17 (2025) 7016–7029, https://doi.org/10.1039/d4nr05002a.
[40] A. Jha, K. Manish, B. Kanchan, M. Manjit, B. Mishra, Biopolymer-based tumor microenvironment-responsive nanomedicine for targeted cancer therapy, Nanomedicine 19 (7) (2024) 633–651, https://doi.org/10.2217/nnm-2023-0302.